Advances in Water Resources 181 (2023) 104546

Contents lists available at ScienceDirect

Advances in Water Resources

journal homepage: www.elsevier.com/locate/advwatres

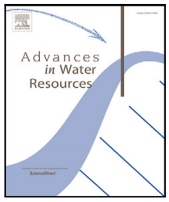

# Numerical investigation of swash–swash interaction effects on beachface evolution using Nonlinear Shallow Water Equations

Fangfang Zhu [a,*], Nicholas Dodd [b]

[a] Department of Civil Engineering, University of Nottingham Ningbo China, Ningbo, 315100, China
[b] Faculty of Engineering, University of Nottingham, Nottingham NG7 2RD, UK

ARTICLE INFO

*Keywords:*
Swash event
Nonlinear Shallow Water Equations
Swash interaction
Beachface evolution

ABSTRACT

This paper presents a numerical investigation of multiple identical swash events to study the swash–swash interaction processes and their impacts on beachface evolution. The numerical model, based on the Nonlinear Shallow Water Equations, is first calibrated/validated against two different single-event-based data-sets. Multiple swash events are generated by identical solitary waves separated by different time intervals, to achieve weak and strong wave-backwash interactions. After a small number of weak interaction events the main feature is erosion from lower and mid swash region and deposition seaward of the swash in a bed-step, created by a backwash bore, primarily due to bed-load. As the number of waves increases, the strength of this backwash bore reduces because of the reduced beach slope caused by the growing bed-step. This eventually leads to a net quasi-equilibrium between bed- and suspended-load per period in most of the swash and surf zones. For strong interaction, initial bed evolution per event is much slower, due to interactions, and is bed load dominated. A quasi-equilibrium is also established as the influence of suspended load grows. Overall bed change per period within the domain eventually converges in both cases. Final bed profiles (i.e. after the same elapsed time, but different numbers of waves) are fairly similar, both with an offshore swash bar. Both profiles continue to evolve on the offshore side of this bar. However, this evolution is driven by suspended load for the weak interactions and bed load for strong interactions. The implication is that similar swash morphological features can emerge from different swash processes, and also be maintained distinctly.

## 1. Introduction

Swash zone beachface evolution plays an important role in the nearshore morphological change, and extensive research efforts have been devoted to this area in the last few decades. Individual physical processes, e.g., bed load, suspended load, ex/infiltration, boundary layer, bore-generated turbulence, in the swash zone have been investigated both experimentally and numerically under one single swash event (Alsina et al., 2009; Kelly and Dodd, 2010; Kikkert et al., 2012; Zhu et al., 2012; Zhu and Dodd, 2013, 2015; Hu et al., 2015; Incelli et al., 2016; Briganti et al., 2016; Perera et al., 2019; Zhu and Dodd, 2020; Pintado-Patiño et al., 2021). In reality, successive swash events interact to varying degrees (Alsina et al., 2016, 2018), and these interactions have been recognised as important in beachface evolution (Chardón-Maldonado et al., 2016; Alsina et al., 2012). Swash–swash interactions lead to energy dissipation, enhanced bed shear stresses and sediment transport (Puleo and Torres-Freyermuth, 2016). Furthermore, they modify the swash period, and also the development of shocks and corresponding morphological features (Brocchini and Baldock, 2008; Alsina et al., 2012).

Cáceres and Alsina (2012) analysed suspended sediment concentration measured in a series of swash events in a large-scale wave flume, and found that the presence of swash–swash interactions controlled the events with the most significant amount of suspended sediment. The swash–swash interactions were classified into 3 categories: wave capture (swash event overtaking a preceding event uprush), weak wave-backwash interaction (uprush of a swash event encountering preceding late backwash, resulting in onshore flow), and strong wave-backwash interaction (uprush of a swash event encountering preceding earlier, stronger backwash, resulting in offshore flow).

Alsina et al. (2016) examined the effect of these interactions on the beach evolution in a laboratory experiment using bichromatic wave groups of varying group period to control the degree of interaction in the swash. Their study indicates that a "breaker bar" forms a little offshore, and that the distance offshore is proportional to the group period. And the larger the group (modulation) period, the more variable the morphological evolution is. In addition, a region of deposition is sometimes observed in the upper swash.

* Corresponding author.
*E-mail address:* fangfang.zhu@nottingham.edu.cn (F. Zhu).

https://doi.org/10.1016/j.advwatres.2023.104546
Received 28 March 2023; Received in revised form 26 September 2023; Accepted 29 September 2023
Available online 12 October 2023

However, these tests control interaction by varying the wave height modulation, so three timescales, wave period, swash period (Baldock and Holmes, 1999), and group period are relevant. If we wish to isolate the effect of interactions only we require identical waves separated by differing durations / periods; this is equivalent to considering an infinitely long modulation period. There are a small number of laboratory studies on swash–swash interactions that utilise two waves only (Chen et al., 2016; Pujara et al., 2015). But these are both on non-erodible beaches. The study of Sumer et al. (2011) utilises an erodible beach, and although their study was focussed on individual waves, up to four identical incoming waves were generated without smoothing the beach. Numerical studies of single events (Zhu and Dodd, 2015) reveal a resulting beach profile that is consistent with observations on real beaches, but do not reveal to what state the beach will evolve for multiple waves.

Two or more solitary waves have been utilised to study the swash interactions in a number of experimental studies, because a train of solitary waves resembles long waves on a beach to a certain degree (Pujara et al., 2015; Wu et al., 2021). In the present study, therefore, we also choose solitary waves to generate prominent swash events and successive swash interactions. We present a numerical simulation of multiple, identical solitary waves impinging on an erodible beach, each with the same type of interaction, in order to see how the beach evolves. This allows us to examine the long-term evolution of a beach under two different kinds of interaction, weak- and strong-backwash interactions (therefore we do not consider uprush interactions, in which a larger wave overtakes a smaller one, which would require differing wave heights). Thus we can identify extremes in resulting beach profiles, corresponding to those different kinds of interactions. Additionally, use of a numerical model allows us to obtain a detailed picture in space and time of the beach evolution, and, in particular, of the shock dynamics.

The paper is organised as follows. In Section 2, we present the model equations. In Section 3, we present the validation of the model against laboratory studies each for one single swash event. We then simulate the multiple swash events in Section 4, and discuss the idealisations and potential limitations of this work in Section 5. Finally, we draw our conclusions in Section 6.

## 2. Model development

This work utilises the model developed by Zhu and Dodd (2015), and the model development is only briefly introduced herein.

### 2.1. Governing equations

The governing equations are the one-dimensional (1D) NSWEs, the Exner equation, and suspended sediment advection equation in which bed and suspended loads due to bed shear stress are included:

$$\hat{h}_{\hat{t}} + \hat{u}\hat{h}_{\hat{x}} + \hat{h}\hat{u}_{\hat{x}} = 0, \tag{1}$$

$$\hat{u}_{\hat{t}} + \hat{u}\hat{u}_{\hat{x}} + g\hat{h}_{\hat{x}} + g\hat{B}_{\hat{x}} = -\frac{c_d \mid \hat{u} \mid \hat{u}}{\hat{h}}, \tag{2}$$

$$\hat{B}_{\hat{t}} + \xi\hat{q}_{\hat{x}} = \xi\left(\hat{D} - \hat{E}\right), \tag{3}$$

$$\left(\hat{h}\hat{c}\right)_{\hat{t}} + \left(\hat{h}\hat{u}\hat{c}\right)_{\hat{x}} = \left(\hat{E} - \hat{D}\right), \tag{4}$$

where $\hat{x}$ represents cross-shore distance (m), $\hat{t}$ is time (s), $\hat{h}$ represents water depth (m), $\hat{u}$ is a depth-averaged horizontal velocity ($ms^{-1}$), $\hat{B}$ is the bed level (m), $\hat{c}$ is the depth-averaged SSC ($m^3/m^3$), $c_d$ is a dimensionless drag coefficient, $\hat{q}$ is sediment flux due to bed load ($m^2s^{-1}$), $\hat{E}$ is the dimensional erosion (or entrainment) rate ($ms^{-1}$) due to bed shear stress, and $\hat{D}$ is the dimensional deposition rate ($ms^{-1}$). Here, $\xi = \frac{1}{1-p}$ with $p$ being bed porosity, and $g$ is gravity acceleration ($ms^{-2}$). Some of the above variables are illustrated in Fig. 1.

We use the following forms for $\hat{q}$, $\hat{E}$ and $\hat{D}$ (Zhu and Dodd, 2015):

$$\hat{q} = \hat{A}\left(\frac{\hat{u}^2}{\hat{u}_0^2}\right)^{3/2}\frac{\mid \hat{u} \mid}{\hat{u}}, \qquad \hat{E} = \hat{m}_e\frac{\hat{u}^2}{\hat{u}_0^2}, \quad \hat{D} = \hat{w}_s\hat{c}, \tag{5}$$

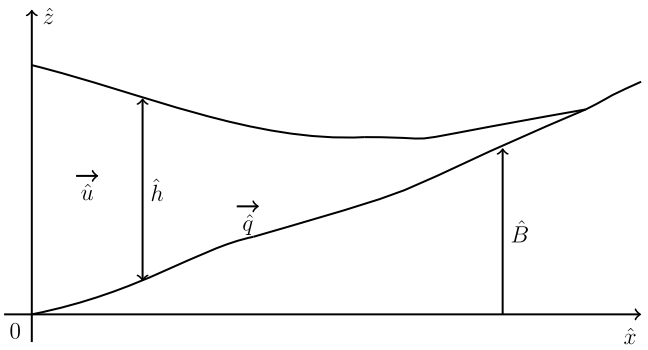


**Fig. 1.** Schematic diagram for a general swash.

where $\hat{A}$ is dimensional bed-load sediment transport rate ($m^2s^{-1}$), $\hat{m}_e$ is the parameter describing the erodibility of the bed ($ms^{-1}$) as suspended load due to bed shear stress, $\hat{w}_s$ is the effective settling velocity of suspended sediment ($ms^{-1}$), and $\hat{u}_0$ is a representative velocity scale ($ms^{-1}$).

Therefore, Eqs. (3) and (4) become:

$$\hat{B}_{\hat{t}} + 3\xi\frac{\hat{A}}{\hat{u}_0^3}\hat{u}^2\hat{u}_{\hat{x}} = \xi\left(\hat{w}_s\hat{c} - \hat{m}_e\frac{\hat{u}^2}{\hat{u}_0^2}\right), \tag{6}$$

$$\left(\hat{h}\hat{c}\right)_{\hat{t}} + \left(\hat{h}\hat{u}\hat{c}\right)_{\hat{x}} = \left(\hat{m}_e\frac{\hat{u}^2}{\hat{u}_0^2} - \hat{w}_s\hat{c}\right). \tag{7}$$

### 2.2. Non-dimensionalisation

We follow the non-dimensionalisation in Zhu and Dodd (2020). The non-dimensional variables are:

$$x = \frac{\hat{x}}{\hat{h}_0}, t = \frac{\hat{t}}{\hat{h}_0^{1/2}g^{-1/2}}, h = \frac{\hat{h}}{\hat{h}_0}, u = \frac{\hat{u}}{\hat{u}_0}, B = \frac{\hat{B}}{\hat{h}_0}, \text{ and } c = \frac{\hat{c}}{\hat{c}_0} \tag{8}$$

where $\hat{h}_0$ is a length scale, $\hat{c}_0 = \frac{\hat{m}_e}{\hat{w}_s}$ is a reference concentration and $\hat{u}_0 = (g\hat{h}_0)^{1/2}$.

Using Eq. (8), Eqs. (1) and (2) become

$$h_t + uh_x + hu_x = 0, \tag{9}$$

$$u_t + uu_x + h_x + B_x = \frac{c_d \mid u \mid u}{h}. \tag{10}$$

Substituting Eq. (8) into Eqs. (6) and (7) gives

$$B_t + 3\xi\frac{\hat{A}}{\hat{h}_0(g\hat{h}_0)^{1/2}}u^2u_x = \xi\frac{\hat{m}_e}{(g\hat{h}_0)^{1/2}}\left(c - u^2\right), \tag{11}$$

$$(hc)_t + (huc)_x = \frac{\hat{w}_s}{(g\hat{h}_0)^{1/2}}\left(u^2 - c\right). \tag{12}$$

Letting

$$\sigma = \xi\frac{\hat{A}}{\hat{h}_0(g\hat{h}_0)^{1/2}}, M = \xi\frac{\hat{m}_e}{(g\hat{h}_0)^{1/2}}, \text{ and } w_s = \frac{\hat{w}_s}{(g\hat{h}_0)^{1/2}},$$

Eqs. (11) and (12) are simplified to:

$$B_t + 3\sigma u^2u_x = M\left(c - u^2\right), \tag{13}$$

$$(hc)_t + (huc)_x = w_s\left(u^2 - c\right). \tag{14}$$

Eqs. (9), (10), (13) and (14) can be rewritten in characteristic form such that we have 4 Riemann equations along 4 characteristics

$$\frac{dx}{dt} = \lambda_i \quad \text{for} \quad i = 1, 2, 3, 4. \tag{15}$$

Among the 4 characteristics, $\lambda_1 < \lambda_3 < \lambda_2$, where $\lambda_1 < 0$ and $\lambda_2 > 0$, and $\lambda_4 = u$. See Zhu and Dodd (2015, 2020) for more information.

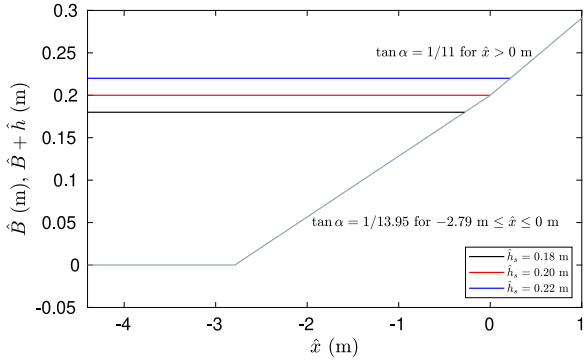


**Fig. 2.** Initial conditions of the Alsina et al. (2009) swash event.

### 2.3. Shock conditions

Applying mass and momentum conservation across a shock, i.e., a bore, gives the Rankine–Hugoniot conditions:

$$-W(h_R - h_L) + (h_R u_R - h_L u_L) = 0, \tag{16}$$

$$-W(h_R u_R - h_L u_L) + \left(h_R u_R^2 + \frac{1}{2}h_R^2 - h_L u_L^2 - \frac{1}{2}h_L^2\right) + \frac{1}{2}(h_R + h_L)(B_R - B_L) = 0, \tag{17}$$

$$-W(B_R - B_L) + \sigma(u_R^3 - u_L^3) = 0, \tag{18}$$

$$-W(h_R c_R - h_L c_L) + (h_R u_R c_R - h_L u_L c_L) = 0, \tag{19}$$

where the subscripts $L$ and $R$ represent the left and right sides of the bore, and $W$ is the shock velocity.

### 2.4. Seaward boundary treatment

The seaward boundary conditions are absorbing-generating, in which the incoming wave is defined, and the outgoing one is estimated. The water depth $h$, velocity $u$, bed level $B$ and SSC $c$ at the seaward boundary are calculated following the technique in Incelli et al. (2015).

## 3. Model validation and calibration

We choose two data-sets to validate the present model against, both of which examine a single swash event, and thereby avoid problems with wave absorption, spurious low-frequency wave generation etc. These are Alsina et al. (2009), in which suspended load is measured, and Sumer et al. (2011), in which final bed change is measured.

### 3.1. Validation against Alsina et al. (2009)

#### 3.1.1. Initial and boundary conditions

The initial conditions are shown in Fig. 2. The section $-4.14$ m$\leq \hat{x} \leq 0$ m is mobile, of median grain size $\hat{D}_{50} = 0.183$ mm, a bulk density of 1641.92 kgm$^{-3}$, and sediment porosity 0.34, and other sections are rigid. The beach has two slopes: 1/13.95 for the region $-2.79$ m$\leq \hat{x} \leq 0$ m (the mobile bed), and 1/11 for $x > 0$ m (immobile bed). There are three tests: test d18 of still water depth $\hat{h}_s = 0.18$ m, and shoreline position $\hat{x} = -0.279$ m; test d20, $\hat{h}_s = 0.20$ m and $\hat{x} = 0$ m, and test d22, $\hat{h}_s = 0.22$ m and $\hat{x} = 0.22$ m. See Alsina et al. (2009) for more information.

The simulations are driven by the measurements of free surface elevation $\hat{\eta}$ at $\hat{x} = -4.4$ m, which are of broken solitary waves of heights 0.129, 0.127 and 0.12 m for tests d18, d20 and d22 respectively. The water depth can be calculated $\hat{h} = \hat{h}_s + \hat{\eta}$.

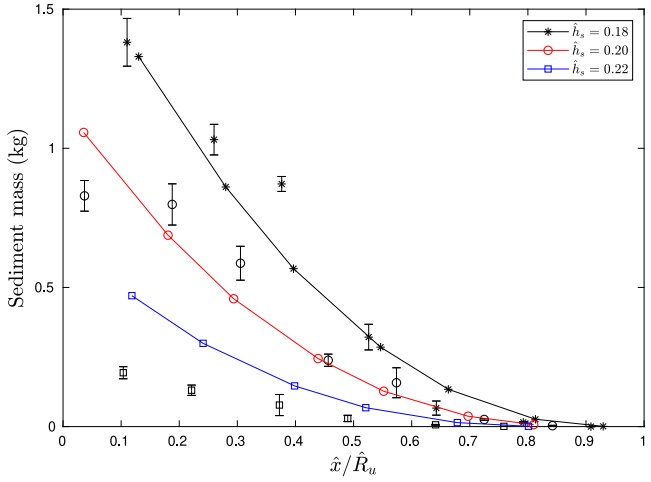


**Fig. 3.** Cross-shore distribution of the present modelled (lines with symbols) and measured (symbols with error bars) sediment mass in the swash zone. $R_u$ is the maximum horizontal run-up distance.

#### 3.1.2. Results comparison

The comparison of cross-shore distribution of suspended sediment against Alsina et al. (2009) with $M = 3 \times 10^{-3}$, $w_s = 0.0046$ (corresponding to $\hat{w}_s = 0.0143$ ms$^{-1}$ for $\hat{D}_{50} = 0.183$ mm), and $c_d = 0.005$ (chosen to match maximum run-up) is shown in Fig. 3. The results are qualitatively and quantitatively close to the measurements. The numerical prediction overpredicts the sediment mass in the $\hat{h}_s = 0.22$ m case, which is consistent with the numerical results obtained by Alsina et al. (2009). A possible explanation may be that both models omit a threshold of movement, which, for the deeper water / smaller mobilisation experiments, would be more significant.

The percentages of sediment in the sediment traps to the initial pre-suspended sediment illustrated in Fig. 4 demonstrate close agreement of modelled results with the experimental data and also the modelled data from Alsina et al. (2009).

Note that bore-generated turbulence is not included in the present simulation, but is considered in the numerical model of Alsina et al. (2009). However, the modelled results in this work are generally close to the experimental data, and also to the modelled data from Alsina et al. (2009). This could be because entrainment due to bore-generated turbulence is limited for this experiment, although in their experiment (Alsina et al., 2009) identify the region in which the bore turbulence encounters the bed as exclusively the region in which suspension occurs and bed change happens (p.630); alternatively, the bed shear stress entrainment term within the present numerical model may provide a similar physical entrainment mechanism under these single swash events as the bore turbulence term.

### 3.2. Calibration against Sumer et al. (2011)

The experimental set-up of Sumer et al. (2011) is shown in Fig. 5. Several solitary waves of wave height $\hat{H} = 0.071$ m first propagate over a flat, erodible beach of still water of depth $\hat{h}_s = 0.4$ m, and then climb up an erodible beach of slope $1 : 14$. The seaward boundary in the numerical simulation is set at the beach toe where $x = 0$ m. The first solitary wave signal is defined as

$$\hat{\eta} = \hat{H}\,\mathrm{sech}^2\,(\hat{\omega}(\hat{t} - 7.98)), \tag{20}$$

for $\hat{t} \geq 0$, where

$$\hat{\omega} = \sqrt{\frac{3}{4}\frac{\hat{H}}{\hat{h}_s^3}}\sqrt{g(\hat{h}_s + \hat{H})}. \tag{21}$$

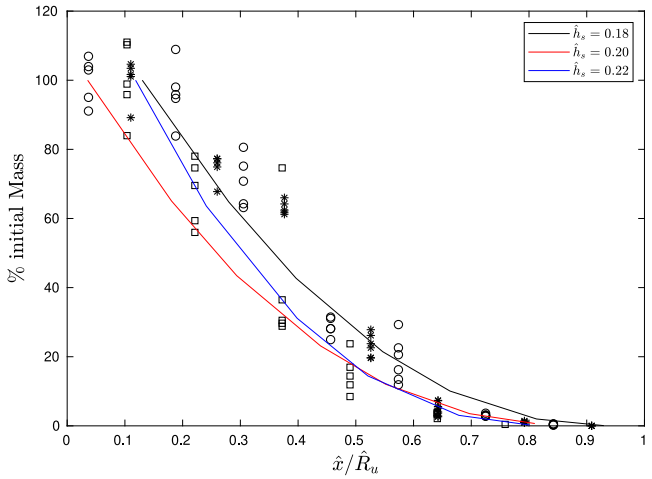


**Fig. 4.** Cross-shore distribution of the percentage of the initial pre-suspended sediment within the swash zone. Modelled: lines; and measured: symbols. Stars represent test d18, circles test d20, and squares test d22.

The beach is of sediment size of $D_{50} = 0.18$ mm, which is very similar to that of Alsina et al. (2009). This therefore provides us with some justification to re-use the suspended sediment mobility from the earlier validation, and use the present experiment to calibrate the bed load mobility. From the sediment size $D_{50}$, $\hat{w}_s = 0.0139$ ms$^{-1}$ ($w_s = 0.0051$) is calculated. Here we set $c_d = 0.005$.

The time interval between two consecutive solitary waves is set to 15.96 s such that the wave interactions between the consecutive waves are weak.

For comparison we plot Fig. 6(a), which shows the bed changes after 4 events including suspended-load only, and so neglecting bed-load transport, using $M = 3 \times 10^{-3}$ and $\sigma = 0$ (the parameters used for the Alsina et al. (2009) validation). In Fig. 6(b), in contrast, we show the equivalent calculation including both bed- and suspended load, as defined for this simulation. The present model (for $\sigma = 6 - 8 \times 10^{-3}$) gives quantitatively similar reproduction of net bed change after four solitary wave events as that observed in the experiments. The obvious discrepancy is the positive bed change observed near $\hat{x} = 1$ m. This is not reproduced by the Navier–Stokes simulation of Li et al. (2019) either, results from which are also shown in Fig. 6(b).

## 4. Swash simulation

In this section, we simulate multiple swash events driven by a varying number of identical solitary waves of height 0.6 at the seaward boundary ($x = 0$) over an erodible plane beach of initial slope 1/15, corresponding to a beach slope on which bore-driven swash is likely to exist. We set $D_{50} = 0.27$ mm ($\hat{w}_s = 0.034$ m/s), which corresponds roughly to the lower range of medium grain sand (Soulsby, 1997), and $c_d = 0.01$, consistent with a slightly rougher bed and with Zhu and Dodd (2015).

Here, instead of using $\sigma$ and $M$ values from the preceding validations, we choose to set $\sigma = 0.01$ (slightly larger than the maximum $\sigma$ of the Sumer et al. (2011) calibration), and $M = 0.001$ (one third the value used in the calibrations), in order to be consistent with Zhu and Dodd (2015) (whose values themselves emerged by calibrating against a field data-set).

The time interval, $T_I$, between two consecutive wave crests (i.e. the wave period) is varied to achieve different swash–swash interactions: $T_I > T_s$; where $T_s$ is the swash period (see Baldock and Holmes, 1999), for weak wave-backwash interaction; and $T_I < T_s$ for strong wave-backwash interaction. Therefore, two $T_I$ values are used: $T_I = 20$ for strong swash–swash interactions, and $T_I = 90$ for weak swash–swash interactions. This combination of solitary wave and beach slope yields $T_s = 45$, $\Rightarrow T_I/T_s = 2$ for weak interaction, and $T_I/T_s = 0.44$ for strong interaction.

The tests utilise two or more solitary waves. The peaks of the waves occur at $t = 10 + (n-1)T_I$, where $n = 1, 2, \ldots$ represents the number of waves. In the simulations for the strongly interacting waves, the initial wave ($n = 1$) does not interact with a preceding backwash. Therefore, we ignore this wave in our analysis by considering the first interacting swash event (from wave $n = 2$) to start at $t = 40$, and the bed assumed to start to change from $t = 40$ (when wave $n = 2$ is about 4 m from the initial shoreline). The second strongly interacting swash event is then due to wave $n = 3$.

### 4.1. Initial conditions

Identical initial conditions to those in Zhu and Dodd (2020) are utilised. The domain extends from $x = 0 - 30$; $h = 1$ for $0 < x < 4$, and the 1/15 beach slope extends from $x = 4$ to 30 $\Rightarrow$ the initial shoreline is at $x = 19$. Water is still ($u(x, 0) = 0$) and devoid of sediment ($c(x, 0) = 0$), and free surface $\eta = h + B = 1$.

### 4.2. Two waves

#### 4.2.1. Flow dynamics

The contour plots for water depth $h$ and velocity $u$ for the simulations of 2 waves with $T_I = 90$ and 20 are shown in Fig. 7. The corresponding contour plots for bed change $\Delta B$ and SSC $c$ are shown in Fig. 8.

When $T_I = 90$ (weak interaction), the two consecutive swash events have very weak interaction. Therefore in the second event we see an almost identical flow and suspended sediment field (Figs. 7 and 8, upper panels). The second incoming bore is almost identical to the first, while the backwash bore is slightly changed. Differences in the second event are primarily observed in the bed change (Fig. 8(a)), although most change is repeated in the second event. Note that the second uprush smoothes the pre-existing, discontinuous bed step (see Fig. 9), but this continuous bed-form remains in place. Fig. 9 shows that as the uprush flow passes the bed-step feature, the free surface rises at the bed-step and drops away from the bed-step, forming a local elevation in the free surface.

In the strong interaction case ($T_I = 20$), the $n = 2$ and 3 incoming bores interact strongly with the backwash flow from the preceding events. Thus, there is no backwash bore development for either wave. These waves both encounter receding flow, with $\max|u| > 0.4$ (Fig. 7(d)), and the interaction results in onshore flow with reduced velocity and momentum. Thus, higher backwash velocities only pertain for reduced durations. The maximum inundation of these strongly-interacting bores is substantially less than those of weakly interacting swash of identical incoming waves (compare Fig. 7(c,d) with Fig. 7(a,b)), although the flow is deeper.

The SSC in the run-up of the strongly interacting waves is smaller than for the weakly interacting waves (Fig. 8(d) and (b) respectively)). This is because of the deeper flow in the strong interaction case, the shorter durations over which slightly smaller backwash velocities exist, and the smaller velocities on the uprush, which imply less sediment entrainment.

#### 4.2.2. Shock dynamics

The shock paths are also illustrated in Fig. 7. As mentioned, there are two significant shocks observed that contribute to bed change: the incoming bore, and the backwash bore (respectively $\lambda_2$ and $\lambda_3$ shocks Zhu and Dodd, 2015). Only the incoming bore contributes to the strong interaction ($T_I = 20$) swash (Fig. 7(c), (d)), whereas weak interaction swash ($T_I = 90$) (Fig. 7(a), (b)) leads to both incoming and backwash bores.

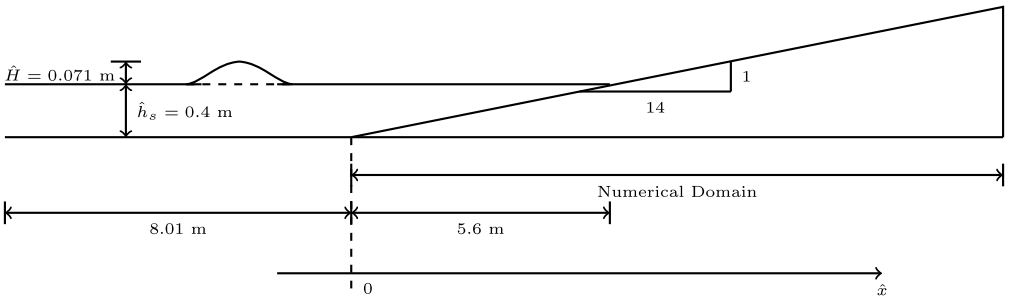


**Fig. 5.** The initial set up of the Sumer et al. (2011) swash event.

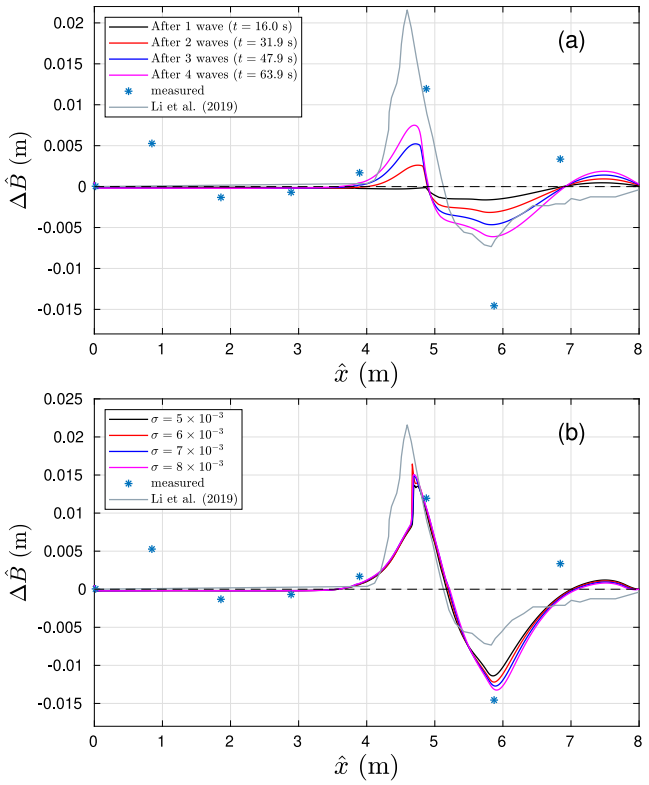


**Fig. 6.** Computed bed change from the present model (a) after 1 to 4 events, using parameters used for Alsina et al. (2009) simulation ($c_d = 0.005$, $M = 3 \times 10^{-3}$, $\sigma = 0$). (b) after 4 waves, using $c_d = 0.005$, $M = 3 \times 10^{-3}$, and $\sigma = 5 - 8 \times 10^{-3}$. Also shown are the bed level changes measured after 4 waves (∗), and those computed (also after 4 waves) using a Navier–Stokes solver coupled to Exner equation (Li et al., 2019).

In Fig. 10(a–c), water depths, velocities, and bed level differences associated with the second ($n = 2$) (third ($n = 3$)) incoming bore in the weakly (strongly) interacting case, are shown. For weak interaction ($T_I = 90$) the shock propagates into very shallow, very slowly retreating water (red dashed lines). There is a clearly identifiable swash collapse point ($x \approx 19$, see Fig. 10(b)), and, shoreward of that point, small water depths (see Fig. 10(a)). There are large shoreward velocities in lee of the bore (Fig. 10(b)). In contrast, for strong interaction ($T_I = 20$), the incoming bore propagates into deeper water that is still retreating with significant speed (black dashed lines, Fig. 10(a, b)). These result in significant retardation in the incoming bore, no recognisable collapse point, and deeper water and small onshore velocities in lee of the bore.

The strong interaction can also be seen in Fig. 10(d), in which the corresponding incoming bore energy decay rates, calculated using the expression of Zhu and Dodd (2020), are shown. The second peak in the strongly interacting case is the interaction of the incoming bore with the preceding backwash.

Sediment concentration is continuous across shocks. The effect of the incoming bore on $c$ can best be observed in Fig. 8, which shows the flow contours and bore paths. For strong interaction ($T_I = 20$) the incoming bore propagates into water already containing much entrained sediment, and so there is no significant entrainment in lee of the bore. In contrast, for $T_I = 90$ the bore propagates into water with small $c$, leading to a rapid and intense entrainment after bore collapse.

The instantaneous bed change caused by the incoming bore is (in the absence of bore entrainment by turbulence Alsina et al., 2009; Zhu and Dodd, 2020), in both cases due to the change in bed load sediment transport across the shock (Fig. 10(c)), via shock relation (18). For the weak interaction case ($T_I = 90$) there is a significantly larger bed change at the incoming bore, due to the larger change in velocity across it. This bed change can be compared to that caused by the backwash bore (for the weak interaction case) in Fig. 10(e), for $n = 1$ and 2 waves. The maximum bed change at both backwash bores is over four times as large as that at the incoming bores.

#### 4.2.3. Bed change due to swash events

The bed changes after the two weakly interacting, and two strongly interacting waves are shown in Fig. 11 (also shown are the bed changes after one such wave).

The weak interactions allow the backwash bore to develop, which creates the bed-step in the lower swash: see Fig. 11(a). Bed-load creates the bed-step (see Fig. 11(b); see also Zhu and Dodd, 2015), and is responsible for intense erosion centred at the initial shoreline. Suspended load creates a broader erosive region, also centred at the initial shoreline (Fig. 11(b)) and a region of deposition seaward of the bed-step, and in the upper swash. In the weak interaction case, the bed change pattern after 2 waves is similar to that after 1 wave but with larger magnitude.

For strong interaction, the absence of run-up onto a dry or nearly dry beach, and of intense, prolonged backwash leads to the absence of intense erosion in the lower swash, and of the bed-step. Accordingly, bed change is more limited overall. Bed load contributes to a broad region of deposition seaward of the lower swash, and erosion further onshore, while bed change due to suspended load is very limited. Note that in this case there is still water covering much of the bed, with sediment still suspended, although not enough to change the observed patterns significantly. Note also the small peak in deposition at $x \approx 16$, chiefly due to bed load (Fig. 11(b)). This is created by the convergence of bed-load in the backwash, which is a weaker process of bar formation than the backwash bore of non-interacting swash.

The bed change pattern due to suspended load for the strongly interacting waves, which is barely visible in Fig. 11(b), differs from that for weakly interacting waves especially in the upper swash zone region. There the deposition by weakly interacting swash, is replaced by slight erosion. This is a result of less settlement because of larger suspended sediment carrying capacity in strongly interacting case.

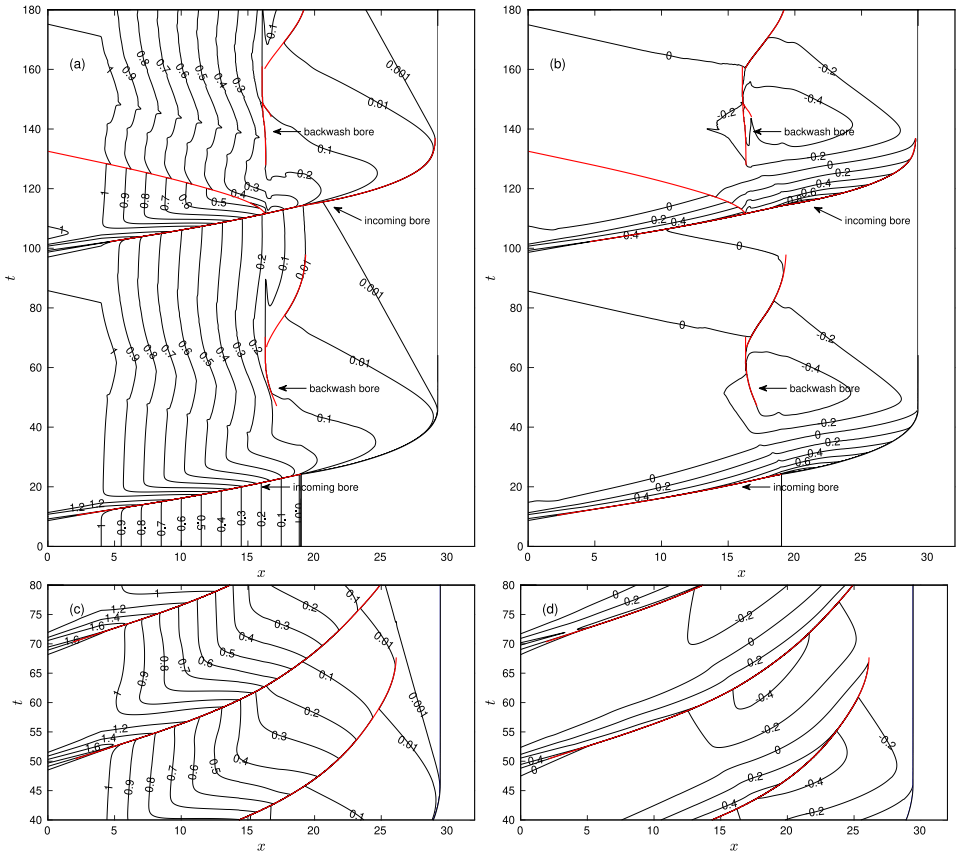


**Fig. 7.** Contour plots of water depth $h$ (a, c) and velocity $u$ (b, d) for the simulations of 2 waves with $T_I = 90$ (upper) and $T_I = 20$ (lower). The red lines represent the shock paths.

### 4.3. Multiple waves

In Fig. 12(a) and (b) we show the accumulated change in bed level at the end of every wave period during 100 weakly and 100 strongly interacting waves.

The evolving bed for the weakly interacting swash events (Fig. 12(a)) exhibits a region of weak deposition in the upper swash, and two, more pronounced regions of bed level change: erosion in the lower swash, mostly shoreward of the initial shoreline; and deposition seaward of the initial shoreline, within which the bed-step occurs (its position within this region varies, and the discontinuous bed-step is now transformed into a continuous morphological feature, primarily due to the settling of suspended load seaward of the step associated with more tranquil flow on the seaward side of the backwash bore.).

The bed change pattern after 100 waves for the strongly interacting event (Fig. 12(b)) has some similarities with the weak interaction case: erosion from the swash region, and deposition further offshore at roughly the same location as the bed-step for the weakly interacting swash. But these regions are now more separated, by a region of relatively little change. The bed-step feature is formed by the converged bed-load transport in the backwash.

Another difference between the two cases is the rate of bed change. After 10 waves (horizontal, dashed black lines in Fig. 12(a), (b)), the maximum deposition (erosion) for strong interaction is about 6 (10) times less than that for the weakly interacting events. After 100 waves, however, the maximum deposition (erosion) in the strongly interacting case is 78% (39%) of that of the weakly interacting case. Thus, with larger numbers of waves the amounts of bed change become more comparable.

To understand these changes better we plot the accumulated bed change due to bed- and suspended load after 10 and 100 periods in Fig. 12(c), (d). The bed- and suspended-load contributions after 10 weakly-interacting waves are strongly reminiscent of those after just one or two (Fig. 11). Bed change due to strongly interacting swash has increased compared to the weak swash but is still smaller and bed load dominated.

After 100 waves (Fig. 12(d)) the accumulated change reveals a different picture for both types of swash. For weakly interacting swash bed change due to bed load suspended- and bed-load-induced bed change now largely oppose each other and are of similar sizes, (except in the offshore region of suspended load deposition), indicating a move towards equilibration. For strongly interacting swash bed load is still dominant, but suspended load is now more prominent, and they are similarly beginning to oppose each other. Maximum bed changes are now more similar to those for the weakly interacting case.

The comparison between Fig. 12(c) and (d) demonstrates that sediment transport mode dominance has moved towards suspended load in between the first 10 waves and the first 100 waves in the weakly interacting swash. The growing offshore bed step feature weakens the backwash, and reduces the asymmetry between uprush and backwash resulting in less bed-load-induced bed change. The overall pattern of suspended sediment is roughly unchanged because it is advected by flow, and less influenced by bed level changes. For strongly interacting swash, the bed change pattern due to bed load remains similar, while that due to suspended load in the upper swash zone changes from erosion into deposition.

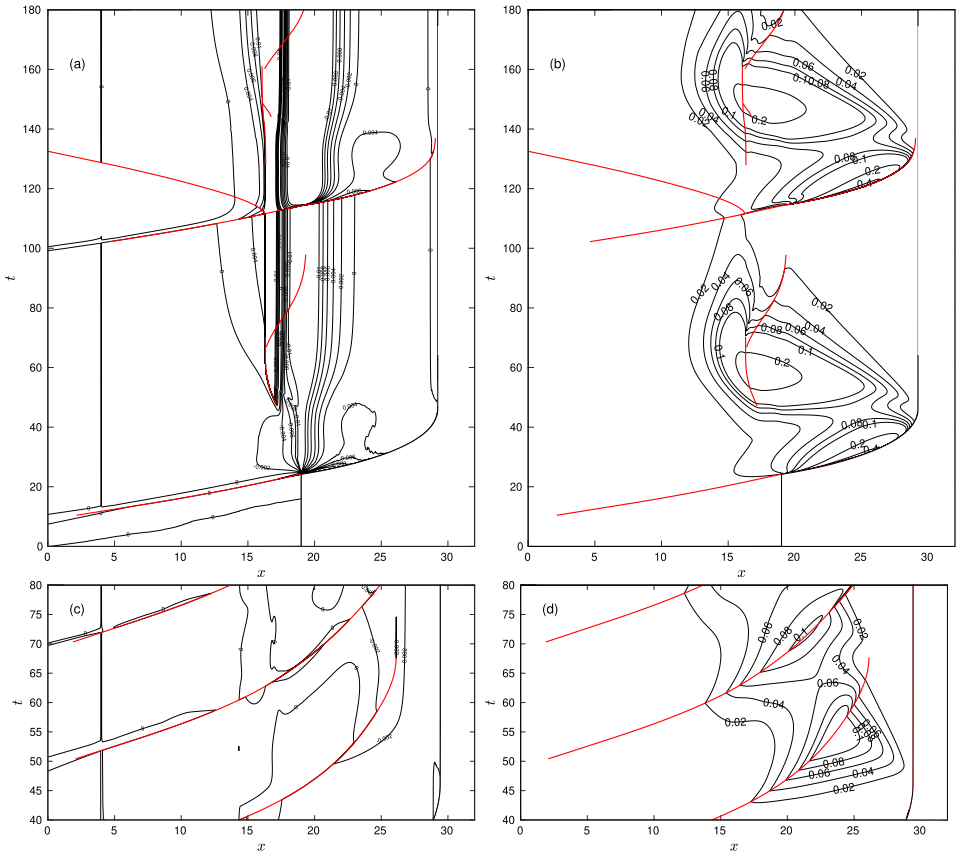


**Fig. 8.** Contour plots of bed change $\Delta B$ (a, c) and SSC $c$ (b, d) for the simulations of with $T_I = 90$ (upper) and $T_I = 20$ (lower). The red lines represent the shock paths.

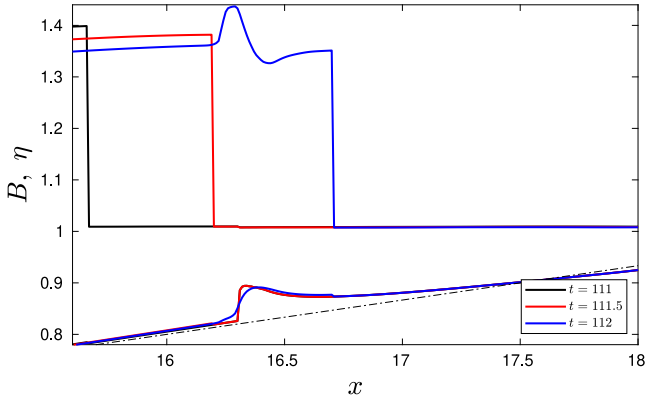


**Fig. 9.** Flow structures around the bed step when the second incoming bore passing the bed step in $T_I = 90$.

#### 4.3.1. Quasi-equilibrium

For the weakly interacting waves the major reason for the slowing down of bed change is the negative feedback of bed change on the backwash bore. As the deposition due to the backwash bore grows, the local offshore beach slope decreases, which reduces the backwash velocity, which, in turn, decreases the backwash bore strength, see Fig. 13; note that the bed change due to the incoming shock (also Fig. 13) remains almost identical in size.

The quasi-equilibrium can be seen more clearly in Fig. 14(a) in which bed change in the weak interaction case due to bed- and suspended-load sediment transport (grey lines), and total sediment transport (black line) over only the 100th period is shown. In the swash region ($20 \lessapprox x \lessapprox 28$) there is a quasi-equilibrium: erosion (deposition) by bed- (suspended-) load in the upper swash, and deposition (erosion) by bed- (suspended-) load in the lower swash. This balance happens because (suspended load) the larger shoreward velocities at bore collapse entrain much sediment on the uprush, which is deposited via settling lag in the upper swash; velocities on the backwash are not large enough to undo this. For bed-load bore collapse leads to intense spatial gradients and uprush erosion in the lower swash and modest deposition in the upper swash; but the larger backwash duration, and, especially, the backwash bore (which, though diminished, is still present), more than reverse the uprush signature. The result may be viewed as a classic morphodynamic swash signal.

In the surf zone (Fig. 14(a)), $x \lessapprox 20$) an inverted morphodynamic signal exists: deposition (erosion) by bed- (suspended-) load in the inner surf zone ($15 \lessapprox x \lessapprox 20$), and erosion (deposition) by bed- (suspended-) load in the outer surf zone ($4 \lessapprox x \lessapprox 15$). The bed-load signature there is due primarily to the incoming bore, which strips sediment in the outer surf zone, and deposits it prior to bore collapse. Sediment is entrained as suspended load in the inner surf zone as the bore impinges on the beach; deposition in the outer surf zone occurs due to settling out of suspension at the end of the cycle, prior to the next wave arriving. Only in the outer surf zone does deposition by suspended load predominate, and there is dis-equilibrium there.

Fig. 14(b) depicts the equivalent plot for strong interactions, but here for the 450th period, which corresponds to the same elapsed time. Here, in contrast, there are three distinct morphodynamic swash signals, separated by regions in which there is little net bed change by mode. These inert regions are those in which interactions reduce velocities (see velocity envelope in Fig. 14(b)). Only seaward of the

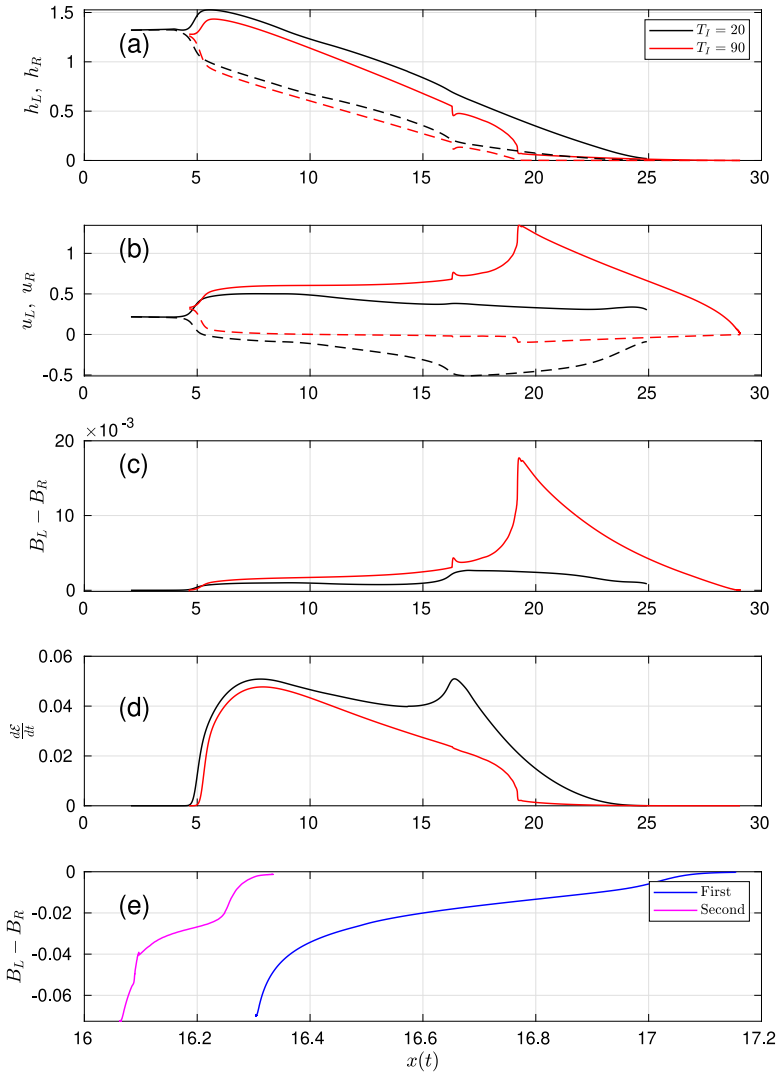


**Fig. 10.** (a) Water depths, and (b) velocities, either side of second weakly (black) and third strongly (red) interacting incoming bore (L = solid lines; R = dashed lines); (c) differences in bed levels across those bores. (d) Incoming bore energy loss, $\frac{d\mathcal{E}}{dt}$, against $x(t)$, the bore path, for the second weakly interacting ($(n = 2)$) and strong incoming ($n = 3$) bores. (e) Differences in bed levels across the first and second backwash bores in the weak interaction case.

most seaward such signal do we see disequilibrium, where deposition by bed-load occurs. This sharp peak in bed-load deposition at $x \approx 12$ is typical of a backwash bore (i.e. a morphodynamical or $\lambda_3$ bore Zhu and Dodd, 2015), and, indeed, one does develop at about $t = 600$, which grows to $\Delta B \approx 0.0075$ by $t \approx 4000$, and diminishes thereafter.

An overall magnitude of bed change per period within the domain, $\|\Delta B\|$ can be defined as:

$$\|\Delta B\|(t) = \left\{ \frac{1}{L_x} \int_{x_0}^{x_s} \left( B(x,t) - B(x,t-T_I) \right)^2 \, dx \right\}^{1/2} \tag{22}$$

(see e.g. Garnier et al., 2010), where $L_x = x_s - x_0$ is the distance from the offshore boundary to the (non-moving) shoreline (Antuono et al., 2012; Zhu and Dodd, 2013).

In Fig. 15 we plot $\|\Delta B\|$ against elapsed time $t$, rather than number of waves, which gives an idea of how rapidly the beach responds in each case. The 9000 time units corresponds to 100 (450) weakly (strongly) interacting waves. $\|\Delta B\|$ rapidly diminishes for weakly interacting waves (Fig. 15) up to about $t = 900$, which roughly corresponds to the region of strong negative feedback on the backwash bore. Thereafter there is a slower decrease, and a slow decay to a non-zero asymptote.

For strongly interacting waves, in contrast, $\|\Delta B\|$ remains of similar magnitude throughout, and a similar asymptotic behaviour is seen.

#### 4.3.2. Final bed profiles

The final bed profiles after 450 strongly and 100 weakly interacting waves are shown in Fig. 16. Both beach profiles show a comparable amount of total bed change for the same elapsed time (average $|\Delta B| = 0.0489$, and 0.0525, for weakly and strongly interacting waves), but very different numbers of waves. Both profiles also possess a swash bar (region of overall deposition) beginning seaward of the initial shoreline ($x = 19$) and extending further offshore, and primarily erosion in their most shoreward part. The strongly interacting swash profile possesses two local troughs, corresponding to the regions of diminution of the velocity envelope (Fig. 14(b)), which therefore define a smaller bar feature shoreward of the initial shoreline. Both profiles are still evolving only on the offshore section of the swash bar.

## 5. Discussion

The present study is idealised to some extent, and it is useful to consider the implications.

Identical solitary wave trains are utilised because the purpose is to isolate and study the effects of two limiting extremes of wave-driven swash, interacting and non-interacting, and to remove other possibly obscuring effects. Real wave trains will exhibit less uniformity. Wave trains of 100 non-interacting (450 interacting) solitary waves could, in

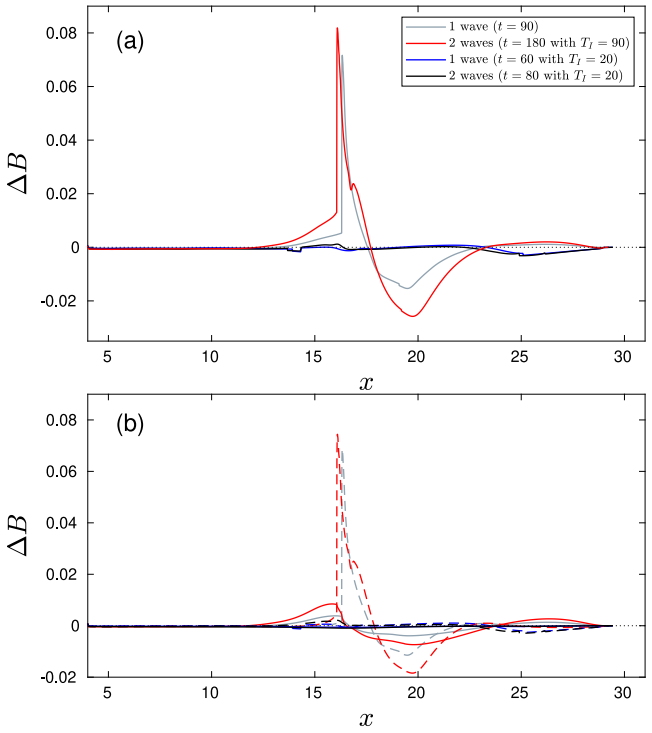


**Fig. 11.** (a) Bed changes after 1 and 2 waves. (b) Contributions by suspended load and bed load after 1 and 2 waves. Solid line: suspended load, and dashed line: bed load.

the field, equate to, say, a duration of ~20 (~40) min of swell (locally-generated) waves. The main differences would be likely to be variations in amplitude, especially for local waves.

We neglect sediment entrainment by bore turbulence, because good comparison with single-event-based data-sets is achieved whilst excluding it. Bore turbulence will suspend sediment prior to bore collapse (Alsina et al., 2009), and its inclusion in the numerical model would result in increased suspended sediment concentration and more deposition in the upper swash zone (Zhu and Dodd, 2020). Because weakly interacting swash can be seen as a series of single swash events, this gives some justification for neglecting its effects for those waves, although it is possible that differences due to its inclusion may accumulate. Field observations of strongly interacting waves (see Cáceres and Alsina, 2012) indicate larger suspended sediment concentrations associated with bore–swash interactions, which may be due to the effects of bore turbulence. Numerical experiments by the present authors incorporating bore turbulence (Zhu and Dodd, 2020) for weak and strong interactions (not shown) confirm both the above points from the numerical modelling perspective: it is unimportant for weak interactions, and it is relatively important for strong interactions. However, the inclusion of entrainment by bore turbulence in numerical models needs further assessment by laboratory or field measurements in which the role of bore turbulence can be isolated from other effects, so that we can determine its importance, and thus determine if present models do indeed accurately capture its effects.

We also exclude downslope diffusion of sediment here to investigate the importance of the shock dynamics. Its inclusion is likely to smooth out the resulting profiles, as the local angle of repose is exceeded, but is unlikely to make a significant difference to the profiles. We do not consider in/exfiltration. This probably explains the eventual absence of a swash bar on the dry beach (i.e., the swash berm) in the weakly interacting swash. A small dry beach deposition is present initially, due to settling lag effects (Pritchard and Hogg, 2005), but bed-load ultimately counteracts this effect (see Fig. 14(d)). But it is infiltration into the beach in the upper swash that is primarily responsible for berm formation (Masselink and Li, 2001; Dodd et al., 2008); the infiltrating flow is no longer available to mobilise sediment in the backwash. Infiltration is a feature primarily of coarser sand beaches, which are more permeable. So, we would not expect such a feature to be prominent on beaches of the grain size we consider here.

It should also be borne in mind that NSWEs are themselves limited, in that they are strictly representative of flows in which the pressure is hydrostatic, and in which it can be assumed that $u^2 \approx \frac{1}{h}\int_B^{B+h} v^2(x,z,t)\,dz$, where $z$ is the vertical coordinate, and $v$ is the depth-varying cross-shore current. To some extent both these conditions are violated in the swash, particularly where significant vertical velocities exist, e.g. at bore front, at bore interactions and in the vicinity of the swash tip. Nonetheless, the NSWEs have been shown to represent swash flows with a high degree of accuracy (see e.g. Dodd, 1998; Briganti et al., 2011; Zhu et al., 2022; Pourzangbar and Brocchini, 2022).

Despite these idealisations, it is useful to compare the observed final bed profiles to those observed by Alsina et al. (2018). As noted earlier, these experiments were of wave groups. For the shorter group period multiple types of interaction occur (weak-, strong- and wave capture), so they are not directly comparable to the present numerical simulations. However, the present weak interaction final profile is similar to that for the shorter wave group (Fig. 2(a) of Alsina et al. (2018)), especially in the presence of a swash bar. As mentioned, the absence of the berm in the present simulations is probably due to the absence of infiltration, and there being no entrainment from bore turbulence. This better correspondence to the shorter wave group period series may seem curious, because Alsina et al. (2018) note that the shoreline is group period dominated for that case. However, the individual swash events, are visible in the $u$ signature. Moreover, the larger, weakly interacting swash events, as well as those where larger events capture a smaller preceding one, are likely to effect more morphodynamic change per event, as seen in the present simulations for weakly interacting events. In contrast, the longer group period waves result in a swash zone that shifts at the group period, and so these experiments are less comparable to the present numerical ones, even though our experiments are equivalent to wave group experiments with an infinite group period.

## 6. Conclusion

For weakly-interacting swash bed change is strongly influenced by incoming and backwash bores, and is initially bed-load dominated (in particular, the formation of the bed-step by the backwash bore) and rapid. However, negative morphodynamic feedback due to the bed-step created by the backwash bore diminishes the backwash bore, and subsequent bed change is increasingly due, about equally, to bed- and suspended load, and is less rapid. Longer-term bed change (100 waves) yields a quasi-equilibrium over most of the bed profile, with suspended load dominance at the swash bar. The pattern of morphological change that emerges is that of a what we term a classical morphodynamical swash signal in the swash zone: net deposition (erosion) in the lower (upper) swash due to bed-load; net erosion (deposition) in the lower (upper) swash due to suspended load. And an inverted morphodynamic swash signal offshore of that.

For strongly interacting swash the backwash bore does not initially exist, and nor, therefore, does the bed-step. Bed change is initially comparatively slow (compared to weakly-interacting swash) and also bed-load dominated. The bed-load dominance is likely to be related to the overall reduced velocities in this case (see Fig. 14), because suspended load entrainment is directly proportional to velocity, whereas bed change caused by bed-load transport is dependent on both velocity and velocity gradients (see Eq. (13))

The rate of bed change, however, remains similar throughout the evolution. A quasi-equilibrium also is apparent for this case, once more

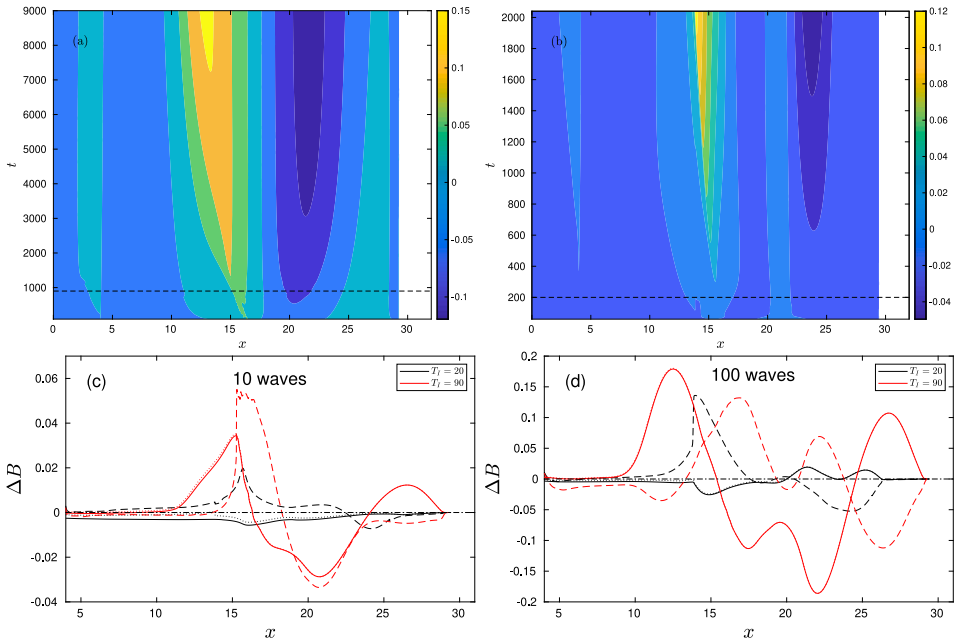


**Fig. 12.** Top: Change in bed levels ($B(t_0 + nT_I) - B(t_0)$) for $n = 1 \ldots 100$: (a) $T_I = 90$ ($t_0 = 0$) (weakly interacting waves) (b) $T_I = 20$ ($t_0 = 40$) (strongly interacting waves). The dashed horizontal line corresponds to the 10th period. Bottom: accumulated contributions to bed change for $T_I = 90$ (red) and $T_I = 20$ (black) by suspended load and bed load after (c) 10 and (d) 100 periods (for $T_I = 20$ change is measured relative to bed profile at $t = 40$). Solid line: suspended load, and dashed line: bed load. Dotted lines: bed level that would result if all suspended sediment at this time were transformed into bed change.

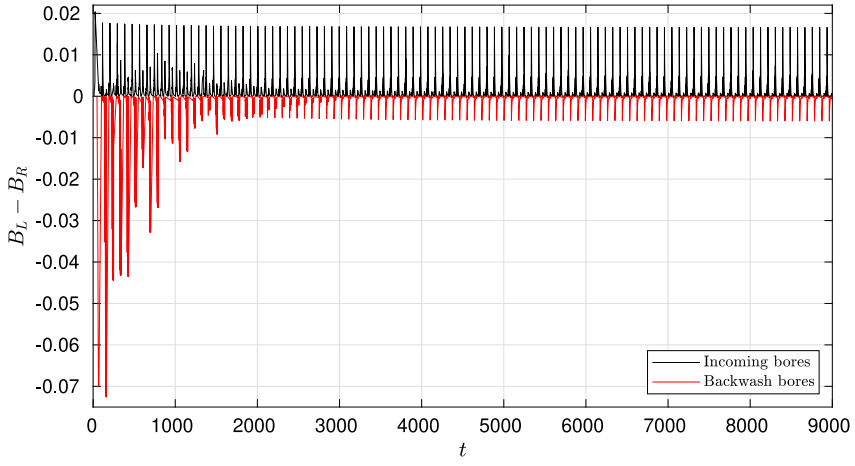


**Fig. 13.** Differences in bed levels ($B_L - B_R$) across all shocks in the 100 wave weak interaction simulation. Negative jumps (red) mostly comprise the backwash bores and positive jumps mostly the incoming bores.

with only the most seaward morphology still evolving. The interactions result in three swash signals separated by regions of reduced velocities that are morphodynamically inert. A morphodynamic shock feature emerges during evolution at the seaward edge of the most seaward swash signal, which forms the main morphologically active part of the beach profile. It emerges because of the convergence of the backwash flow. With the accumulation of water in the swash zone, the backwash flow becomes stronger, and a backwash bore is detected at $t \approx 640$ (the 31st interacting wave). The bed step feature is not smoothed as much as in the weakly interacting case because the flow is not tranquil on the seaward side of the backwash bore, and less deposition there.

Initially, each strongly-interacting event effects less morphological change than each weakly interacting event, up to about $t = 4000$ (200 waves). Thereafter, both types of event result in a similar amount of bed change per period (Fig. 15). Ultimately ($t = 9000$), both profiles exhibit similar amounts of bed change, and an overall similar pattern with an offshore swash bar. Both profiles are still evolving on the offshore side of the swash bar, but by different sediment processes: suspended load (weak interaction case), and bed load (strong interaction). Both sets of interactions therefore yield similar equilibria, but established and maintained in very different ways. The equilibria are dependent on flow features, and it is likely that different mobilities from those chosen here would yield similar equilibrium processes.

The two formation mechanisms of the offshore swash bar and equilibrium process presented in this work represent two extremes of swash/inner surf zone morphodynamical behaviour. They show the dominance of different physical processes at otherwise similar morphological features. Coastal engineering models need to capture both these processes to correctly predict beach behaviour in real seas.

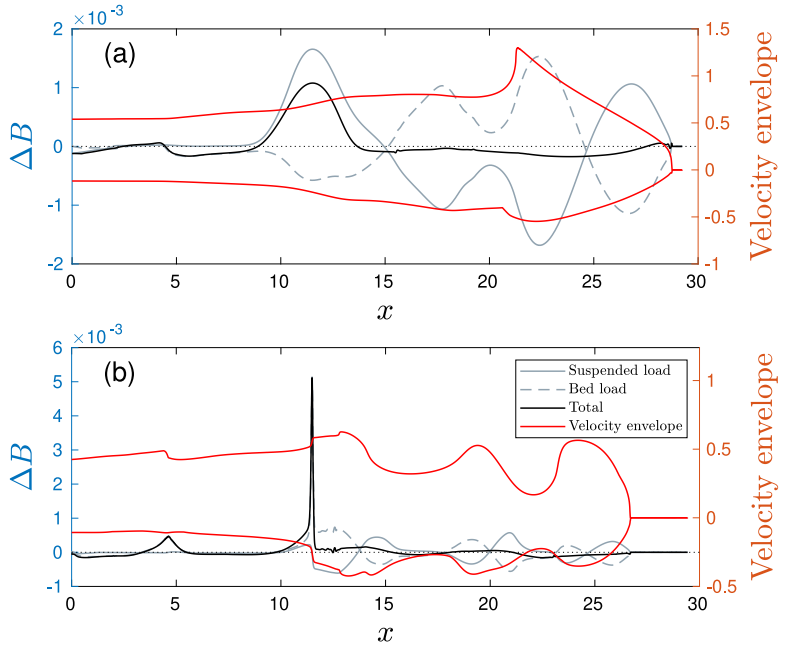


**Fig. 14.** Contributions to bed change for (a): $T_I = 90$ (weak interaction) over only the 100th period; and (b) $T_I = 20$ (strong interaction) over only the 450th period due to bed, suspended and total load. Shown in red (using the right vertical axis) are the depth-averaged velocity envelopes over the 100th (450th) period for the weak (strong) interaction.

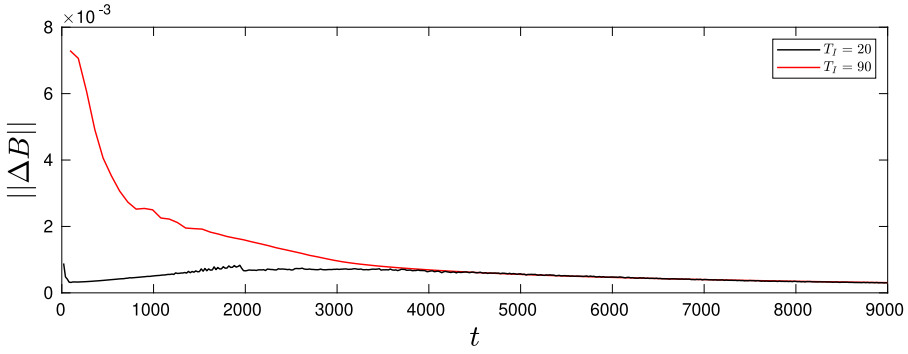


**Fig. 15.** $\|\Delta B\|$ against $t$ for $T_I = 90$ (weakly interacting waves); and $T_I = 20$ (strongly interacting waves).

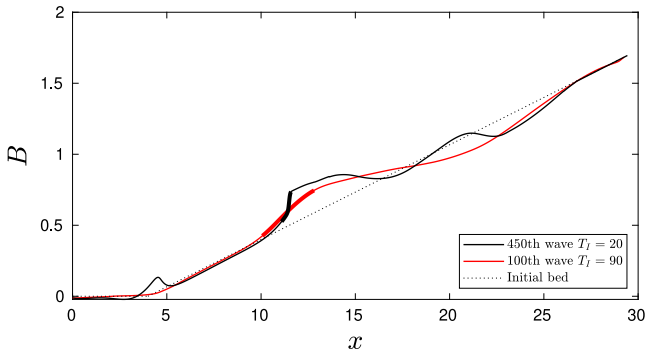


**Fig. 16.** Final bed profiles after 450 strongly and 100 weakly interacting swash events (corresponding to 9000 time units). The bold sections of the profiles indicate those portions for which $|\Delta B| \geq 0.5 \times 10^{-3}$ in the periods immediately prior to the instant at which they are plotted, which therefore indicates the most morphodynamically active part of each profile.

## CRediT authorship contribution statement

**Fangfang Zhu:** Conceptualization, Methodology, Software, Validation, Formal analysis, Data curation, Writing – original draft, Visualization, Project administration, Funding acquisition. **Nicholas Dodd:** Conceptualization, Methodology, Formal analysis, Writing – review & editing, Supervision.

## Declaration of competing interest

The authors declare that they have no known competing financial interests or personal relationships that could have appeared to influence the work reported in this paper.

## Data availability

Data will be made available on request

## Acknowledgements

This work is supported by Natural Science Foundation of China with the project code 51811530012 and 51509135, and also by Ningbo

Natural Science Foundation, China with the project code 2023J190. Dr. José M. Alsina is acknowledged for providing laboratory data for comparison with this study. We are grateful to two anonymous reviewers and the Associate Editor for their comments and suggestions.

## References

Alsina, J.M., Cáceres, I., Brocchini, M., Baldock, T.E., 2012. An experimental study on sediment transport and bed evolution under different swash zone morphological conditions. Coastal Eng. 68, 31–43.

Alsina, J.M., Falchetti, S., Baldock, T.E., 2009. Measurements and modelling of the advection of suspended sediment in the swash zone by solitary waves. Coastal Eng. 56, 621–631.

Alsina, J.M., Padilla, E.M., Cáceres, I., 2016. Sediment transport and beach profile evolution induced by bi-chromatic wave groups with different group periods. Coastal Eng. 114, 325–340.

Alsina, J.M., van der Zanden, J., Cáceres, I., Ribberink, J.S., 2018. The influence of wave groups and wave-swash interactions on sediment transport and bed evolution in the swash zone. Coastal Eng. 140, 23–42.

Antuono, M., Soldini, L., Brocchini, M., 2012. On the role of the Chezy frictional term near the shoreline. Theor. Comput. Fluid Dyn. 26, 105–116.

Baldock, T.E., Holmes, P., 1999. Simulation and prediction of swash oscillations on a steep beach. Coastal Eng. 36, 219–242.

Briganti, R., Dodd, N., Pokrajac, D., O'Donoghue, T., 2011. Non linear shallow water modelling of bore-driven swash: Description of the bottom boundary layer. Coastal Eng. 58, 463–477.

Briganti, R., Torres-Freyermuth, A., Baldock, T.E., Brocchini, M., Dodd, N., Hsu, T.J., Jiang, Z., Kim, Y., Pintado-Patiño, J.C., Postacchini, M., 2016. Advances in numerical modelling of swash zone dynamics. Coastal Eng. 115, 26–41.

Brocchini, M., Baldock, T.E., 2008. Recent advances in modeling swash zone dynamics: Influence of surf–swash interaction on nearshore hydrodynamics and morphodynamics. Rev. Geophys. 46, 1–21.

Cáceres, I., Alsina, J.M., 2012. A detailed, event-by-event analysis of suspended sediment concentration in the swash zone. Cont. Shelf Res. 41, 61–76.

Chardón-Maldonado, P., Pintado-Patiño, J.C., Puleo, J.A., 2016. Advances in swash-zone research: Small-scale hydrodynamic and sediment transport processes. Coastal Eng. 115, 8–25.

Chen, B.T., Kikkert, G.A., Pokrajac, D., Dai, H.J., 2016. Experimental study of bore-driven swash–swash interactions on an impermeable rough slope. Coastal Eng. 108, 10–24.

Dodd, N., 1998. Numerical model of wave run-up, overtopping and regeneration. ASCE J. Water. Port Coast. Ocean Eng. 124 (2), 73–81.

Dodd, N., Stoker, A., Calvete, D., Sriariyawat, A., 2008. On beach cusp formation. J. Fluid Mech. 597, 145–169.

Garnier, R., Dodd, N., Falqués, A., Calvete, D., 2010. Mechanisms controlling crescentic bar amplitude. J. Geophys. Res. 115 (F02007).

Hu, P., Li, W., He, Z., Pahtz, T., Yue, Z., 2015. Well-balanced and flexible morphological modeling of swash hydrodynamics and sediment transport. Coastal Eng. 96, 27–37.

Incelli, G., Briganti, R., Dodd, N., 2015. Absorbing-generating seaward boundary conditions for fully-coupled hydro-morphodynamical solvers. Coastal Eng. 99, 96–108.

Incelli, G., Dodd, N., Blenkinsopp, C.E., Zhu, F., Briganti, R., 2016. Morphodynamical modelling of field-scale swash events. Coastal Eng. 115, 42–57.

Kelly, D.M., Dodd, N., 2010. Beach face evolution in the swash zone. J. Fluid Mech. 661, 316–340.

Kikkert, G., O'Donoghue, T., Pokrajac, D., Dodd, N., 2012. Experimental study of bore-driven swash hydrodynamics on impermeable rough slopes. Coastal Eng. 60, 149–166.

Li, J., Qi, M., Fuhrman, D.R., 2019. Numerical modeling of flow and morphology induced by a solitary wave on a sloping beach. Appl. Ocean Res. 82, 259–273.

Masselink, G., Li, L., 2001. The role of swash infiltration in determining the beachface gradient: A numerical study. Mar. Geol. 176, 139–156.

Perera, E., Zhu, F., Dodd, N., Briganti, R., Blenkinsopp, C.E., Turner, I., 2019. Surface-groundwater flow numerical model for barrier beach with exfiltration incorporated bottom boundary layer model. Coastal Eng. 146, 47–64.

Pintado-Patiño, J.C., Puleo, J.A., Krafft, D., Torres-Freyermuth, A., 2021. Hydrodynamics and sediment transport under a dam-break-driven swash: An experimental study. Coast. Eng. 170, 103986.

Pourzangbar, A., Brocchini, M., 2022. A new process-based, wave-resolving, 2dh circulation model for the evolution of natural sand bars: The role of nearbed dynamics and suspended sediment transport. Coastal Eng. 177, 104192.

Pritchard, D., Hogg, A.J., 2005. On the transport of suspended sediment by a swash event on a plane beach. Coastal Eng. 52, 1–23.

Pujara, N., Liu, P.L.F., Yeh, H.H., 2015. An experimental study of the interaction of two successive solitary waves in the swash: A strongly interacting case and a weakly interacting case. Coastal Eng. 105, 66–74.

Puleo, J.A., Torres-Freyermuth, A., 2016. The second international workshop on swash-zone processes. Coast. Eng. 115, 1–7.

Soulsby, R.L., 1997. Dynamics of marine sands. A manual for practical applications. In: SR. Vol. 466. Hydraulics Research Wallingford., Wallingford, England.

Sumer, B.M., Sen, M.B., Karagali, I., Ceren, B., Fredsöe, J., Sottile, M., Zilioli, L., Fuhrman, D.R., 2011. Flow and sediment transport induced by a plunging solitary wave. J. Geophys. Res. 116, http://dx.doi.org/10.1029/2010JC006435.

Wu, Y.T., Higuera, P., Liu, P.L.F., 2021. On the evolution and runup of a train of solitary waves on a uniform beach. Coastal Eng. 170, 104015.

Zhu, F., Dodd, N., 2013. Net beach change in the swash: A numerical investigation. Adv. Water Resour. 53, 12–22.

Zhu, F., Dodd, N., 2015. The morphodynamics of a swash event on an erodible beach. J. Fluid Mech. 762, 110–140.

Zhu, F., Dodd, N., 2020. Swash zone morphodynamic modelling including sediment entrained by bore-generated turbulence. Adv. Water Resour. 146, 103756.

Zhu, F., Dodd, N., Briganti, R., 2012. Impact of a uniform bore on an erodible beach. Coastal Eng. 60, 326–333.

Zhu, F., Dodd, N., Briganti, R., Larson, M., Zhang, J., 2022. A logarithmic bottom boundary layer model for the unsteady and non-uniform swash flow. Coastal Eng. 172, 104048.